1-1-2014

Ab initio lattice dynamics and electron-phonon coupling of Bi(111)

M. Alcántara Ortigoza
University of Central Florida

I. Yu. Sklyadneva

R. Heid

E. V. Chulkov

T. S. Rahman
University of Central Florida

See next page for additional authors

Ab initio lattice dynamics and electron-phonon coupling of Bi(111)

M. Alcántara Ortigoza,[1,2] I. Yu. Sklyadneva,[3,2,4] R. Heid,[2,*] E. V. Chulkov,[3,5,4,6] T. S. Rahman,[1]
K.-P. Bohnen,[2] and P. M. Echenique[3,5,6]

[1]*Department of Physics, University of Central Florida, Orlando, Florida 32816, USA*
[2]*Institut für Festkörperphysik, Karlsruher Institut für Technologie, D-76021 Karlsruhe, Germany*
[3]*Donostia International Physics Center (DIPC), 20018 San Sebastián/Donostia, Basque Country, Spain*
[4]*Tomsk State University, 6340501, Tomsk, Russian Federation*
[5]*Departamento de Física de Materiales, Facultad de Ciencias Químicas, UPV/EHU, Apdo. 1072, 20080 San Sebastián/Donostia, Basque Country, Spain*
[6]*Centro de Física de Materiales CFM–Materials Physics Center MPC, Centro Mixto CSIC-UPV/EHU, 20018 San Sebastián/Donostia, Basque Country, Spain*

(Received 30 July 2014; revised manuscript received 31 October 2014; published 24 November 2014)

We present a comprehensive *ab initio* study of structural, electronic, lattice dynamical, and electron-phonon coupling properties of the Bi(111) surface within density functional perturbation theory. Relativistic corrections due to spin-orbit coupling are consistently taken into account. Changes of interatomic couplings are confined mostly to the first two bilayers, resulting in superbulk modes with frequencies higher than the optic bulk spectrum, and in an enhanced density of states at lower frequencies for atoms in the first bilayer. We give results for the momentum-dependent electron-phonon coupling of electronic states belonging to the two surface electronic bands along $\overline{\Gamma M}$ which cross the Fermi energy. For larger momenta, the lower surface band exhibits a moderate electron-phonon coupling of about 0.45, which is larger than the coupling constant of bulk Bi. For momenta close to $\overline{\Gamma}$, states of both surface bands show even stronger couplings because of interband transitions to bulk states near $\overline{\Gamma}$ around the Fermi level. For these cases, the state-dependent Eliashberg functions exhibit pronounced peaks at low energy and strongly deviate in shape from a Debye-type spectrum, indicating that an extraction of the coupling strength from measured electronic self-energies based on this simple model is likely to fail.

DOI: 10.1103/PhysRevB.90.195438 PACS number(s): 73.20.At, 68.35.Ja, 63.20.kd, 71.15.Mb

I. INTRODUCTION

Looking back since the advent of modern solid-state physics, bismuth (Bi) has been perhaps one of the most intriguing elements for research. Its singular properties make Bi the metal with the lowest thermal conductivity after mercury and the element with largest diamagnetism. Bi allowed an early discovery of the Seebeck, the de Haas–van Alphen, the Shubnikov–de Haas, and the Nernst effects, all of which are inherently present in metals but were more challenging to observe in general. Bismuth was in fact the first metal whose Fermi surface was experimentally identified [1] and provided the basis to determine that of other metals. Moreover, bulk Bi was the first nonsuperconducting material (at least in the ordered phase) that was found to be superconducting in structurally bulklike nanoparticles [2].

Many of the outstanding properties of bulk Bi are linked to its peculiar electronic structure. Bi is a semimetal with tiny electron and hole pockets and a very small density of states (DOS) at the Fermi level. Metallic screening is therefore much weaker than in typical metals, and the interatomic bonding has a stronger directional component. This connects with the layered crystal structure with alternating weak and strong interlayer bonds, which can be described as a stacking of bilayers. Such structure was explained in terms of a distortion from an ideal cubic structure that derives from a Peierls instability [3]. However, electronic-structure calculations for black phosphorus suggest that a combination of strong mixing of *s* and *p* orbitals and next-nearest-neighbor interaction may also drive the same distortion from the simple cubic structure [4].

Being a semimetal with low DOS at the Fermi energy, bulk Bi is expected to have a small average electron-phonon (*e*-ph) coupling constant λ. Simple estimates based on a tight-binding model [5] as well as a very recent *ab initio* calculation [6] yielded rather small values of $\lambda = 0.13$ and 0.09, respectively, consistent with the finding that Bi does not display superconductivity down to 50 mK [7]. However, since long ago amorphous bulk Bi was found to have a quite strong electron-phonon coupling of $\lambda = 2.46$ (the value is larger than that of amorphous lead [8], which is known to have a strong electron-phonon coupling also in the crystalline form [9]). This indicates that the intrinsic coupling strength of electronic states to the phonons is comparable to those of lead, but superconductivity is only absent due to the very low DOS at E_F.

Interest in surface properties of Bi arises on the one hand from the large difference of the surface electronic structure from the bulk one. Typically, an enhanced metallicity at the surface is observed which is related to the appearance of surface electronic states with an increased DOS at the Fermi energy (E_F) [10]. On the other hand, spin-orbit interaction is strong for Bi, and is a necessary ingredient for even a qualitative description of the electronic structure already for the bulk. On surfaces it invokes large splittings of surface states with deep implications for the Fermi-surface topology. Among the low-index surfaces, Bi(111) is best suited for investigating these properties because it does not break the bilayer structure. This enables the study of modifications in the electronic structure originating in the loss of translational symmetry in a pure form without complications due to additional

*Corresponding author.

breaking of chemical bonds. The surface electronic structure of Bi(111) has been elucidated in a series of photoemission experiments [11–16], which established the enhanced density of charge carriers and the presence of surface states split by spin-orbit interaction. These states create two types of Fermi surfaces, known as hole and electron pockets.

The enhanced DOS at Bi surfaces has stimulated experimental investigations of the coupling strength of surface electronic states. For the Bi(111) surface, Ast and Höchst have estimated the electron-phonon coupling from spectral functions of angular-resolved photoemission spectroscopy (ARPES) measurements assuming a Debye model to account for the spectral shape [14]. The results turned out to be strongly dependent on the cutoff frequency of the assumed Debye spectrum. Fitting the data with a cutoff Debye frequency of 10 meV, appropriate for bulk Bi, yields $\lambda = 0.6$, while assuming a surface Debye frequency of 5 meV yields $\lambda = 2.3$. This strong difference was later ascribed mainly to the limited accuracy of the experiment [17]. An alternative road was pursued by Gayone *et al.*, in which the imaginary part of the self-energy was extracted from the temperature dependence of the linewidth of momentum distribution curves [18]. They found smaller values of $\lambda = 0.40(5)$ for the surface electronic states, albeit still significantly larger than the bulk value.

A prerequisite for a detailed analysis of the electron-phonon coupling at surfaces is the knowledge of the surface vibrational spectrum. In particular, surface localized vibrational modes can couple more strongly to surface electronic states due to their larger spatial overlap [19]. In thin films, it has been shown that important contributions to the coupling may come from optical vibrations [20]. Experimentally, the surface phonon spectrum of Bi(111) has been investigated very recently via inelastic helium atom scattering (HAS) by Tamtögl *et al.* [21,22]. They found a rich spectrum of localized modes, including superbulk modes with frequencies above the maximum bulk frequency.

In view of the experimental uncertainties in extracting reliable numbers for the electron-phonon coupling, theoretical calculations on an *ab initio* basis are highly desirable. The density functional perturbation theory (DFPT) provides a unified scheme to predict electronic, phonon, and electron-phonon coupling properties. However, applications of this technique to bulk Bi and in particular to Bi surfaces are still a challenge because the inclusion of spin-orbit interaction increases the computational effort substantially, especially for calculations of lattice dynamical quantities. Therefore, work along this line was first devoted to the electronic structure. Large splittings of surface bands due to spin-orbit interaction were found for all low-index Bi surfaces by Koroteev *et al.* [16]. In a later work, it was shown that the surface electronic structure of Bi(111) converges very slowly with increasing thickness of the slab, in particular near the zone boundary at $\overline{M}$ [23].

Applications of DFPT to lattice dynamical properties including spin-orbit coupling (SOC) have been devoted first to bulk Bi [24,25]. Díaz-Sánchez *et al.* showed that inclusion of SOC is crucial for an improved agreement between calculation and measurement [25], but it did not provide such a good description as it was the case, for example, for the phonon dispersion of lead [9]. Very recently, DFPT has been used to investigate the lattice dynamics of Bi(111). Due to the numerical effort to include spin-orbit interaction, only slabs up to 6 bilayers could be treated [6,22,26–28], raising the question as to what extent the obtained results represent the surface dynamics in the limit of macroscopically thick slabs. For the 6-bilayer calculation, good agreement with the HAS data was found [22,28].

No attempt has been made so far to address the question of electron-phonon coupling of surface states within such an *ab initio* approach. The aim of this paper is to provide a comprehensive *ab initio* analysis of the electronic structure, lattice dynamics, and electron-phonon coupling of surface electronic states for the Bi(111) surface. Towards this goal, we will also discuss the bulk lattice dynamics, which enters the evaluation of the surface vibrations. As we want to focus on the properties of a semi-infinite surface, we carefully investigate the convergence of the various quantities with increasing thickness of the slabs.

The paper is organized as follows. The computational details are described in the following section. Results are presented and discussed in Sec. III. First, we briefly recapitulate the structure and lattice dynamics of bulk Bi in Sec. III A which is a prerequisite for the surface dynamics study, and present results for the electron-phonon coupling constant. Sections III B to III D are devoted to the structural, electronic, and lattice dynamical properties of the Bi(111) surface, respectively, with emphasis on convergence with respect to the slab thickness. The coupling of surface localized electronic states is then discussed in Sec. III E. Finally, the results are summarized in Sec. IV.

II. COMPUTATIONAL DETAILS

We performed density functional theory (DFT) calculations of bulk Bi and Bi(111) within the local density approximation (LDA) in the parametrization of Hedin and Lundqvist [29]. For the bulk geometry, we also report our results obtained with the PBE variant of the generalized gradient approximation (GGA) [30]. The electron-ion interaction was represented by norm-conserving pseudopotentials in the form proposed by Vanderbilt [31], treating $6s$, $6p$, and $6d$ as valence states. The Kohn-Sham orbitals were expanded in a mixed basis (MB) of local functions and plane waves [32,33]. Spin-orbit coupling was incorporated within the pseudopotential scheme via Kleinman's formulation [34] and used to obtain full charge self-consistency [9].

For convenience, we have chosen the rhombohedral representation of the structure of bulk Bi (which contains two atoms per unit cell) and the hexagonal one [10] to describe the Bi(111) surface. The Bi(111) surface was modeled with slabs having one atom per layer (1×1 in-plane periodicity) and thicknesses of 6 and 12 bilayers. In the calculations involving the surface, a vacuum of 12–14 Å separates the periodic images of the slab to avoid interaction between them. We have used the relaxed system to perform the lattice dynamics calculations.

Integrations over the bulk and surface Brillouin zones (BZ) were performed by sampling $12\times12\times12$ and $12\times12\times1$ meshes corresponding to 189 and 19 irreducible k points for the bulk and surface calculations, respectively, combined with a Gaussian broadening with a smearing parameter of 0.1 eV.

The Kohn-Sham valence states were expanded in a basis set consisting of plane waves with a kinetic energy cutoff of 12 Ry (163 eV) augmented by local s- and p-type functions. The Fourier expansion of the crystal potential and charge density has been found to be safely truncated at 50 Ry. The positions of all atoms in the slab were optimized until the forces on each atom and each direction were smaller than 10^{-3} Ry (2×10^{-2} eV/Å). For this purpose, the Broyden-Fletcher-Goldfarb-Shanno algorithm [35] has been applied. The choice of the parameters has been verified through preliminary tests on the lattice parameters, band structure, volume, bulk modulus, and phonon frequencies at some high-symmetry points of bulk Bi. These tests also showed that the LDA gave more satisfactory results than GGA within our pseudopotential approach. For layered materials with weak van der Waals interaction, LDA frequently provides a better description of the interlayer bonding than GGA [36,37], which is, however, likely due to a fortuitous error cancellation [38]. Yet, Bi does not fall into this class because its interlayer bonding is still metallic.

The calculation of the lattice dynamical matrices at specific q points of the surface BZ (SBZ) was performed using linear-response theory embodied within DFPT [39,40]. Its implementation in the MB scheme is described in Ref. [41]. The dynamical matrices for bulk Bi and Bi(111) slabs were calculated at 189 and 7 irreducible q points, respectively. Real-space force constants were obtained by taking the standard Fourier transform of the corresponding dynamical matrices [42]. The force constants calculated for the Bi(111) slabs were then combined with those of bulk Bi to model the dynamics of much thicker slabs [43]. The force constants for these thick slabs were used to derive the eigenvectors and frequencies of the vibrational eigenmodes of the slab at arbitrary q points of the SBZ. Finally, electron-phonon coupling matrix elements were calculated directly from quantities obtained within DFPT including the contribution from spin-orbit interaction [9].

III. RESULTS AND DISCUSSION

Before discussing the properties of the Bi(111) surface, we first present our results for the structural, lattice dynamical, and electron-phonon coupling properties of bulk Bi.

A. Bulk Bi

The A7 structure that characterizes Bi is a rhombohedral structure containing two atoms per primitive cell. In describing the crystal, one of them (R1) can be considered to lie at the origin and the other one (R2) along the trigonal axis (z axis), as shown in Fig. 1. The rhombohedral representation of the lattice is completely determined by three parameters, the length of its basis vectors a_r, and the two parameters gauging its departure from the simple cubic structure [44] α and u. α denotes the angle between two rhombohedral basis vectors, while u is the internal parameter defining the position of R2 in the primitive unit cell. The crystal can also be viewed as being built from hexagonal planes stacked along the trigonal axis with two alternating distances d_{short} and d_{long}. In terms of the rhombohedral parameters they are given

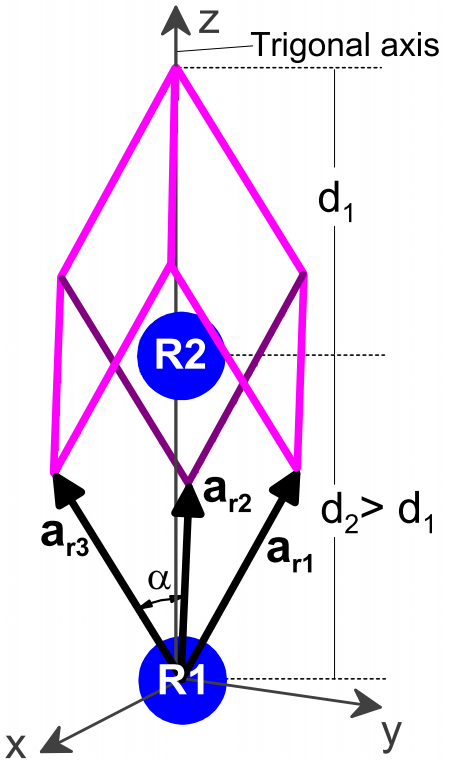

FIG. 1. (Color online) The structure of bulk Bi in the rhombohedral representation (a_r, α, and u are given in Table I), where $\mathbf{a}_{r1} = b\hat{y} + c_r\hat{z}, \mathbf{a}_{r2} = -b(\sqrt{3}/2\hat{x} + 1/2\hat{y}) + c_r\hat{z}, \mathbf{a}_{r2} = b(\sqrt{3}/2\hat{x} - 1/2\hat{y}) + c_r\hat{z}$; $b = a_r\sqrt{2(1-\cos\alpha)/3}$; $c_r = a_r\sqrt{(1+2\cos\alpha)/3}$; $d_1 = 6uc_r$; $d_2 = 3c_r - d_1$. R1 and R2 represent the positions of the two atoms.

by $d_{\text{short}} = (6u-1)c_r$ and $d_{\text{long}} = (2-6u)c_r$, respectively, where $c_r = a_r\sqrt{(1+2\cos\alpha)/3}$ is the length of the basis vectors projected onto the trigonal axis (see Fig. 1). Their ratio is solely determined by u via $d_{\text{short}}/d_{\text{long}} = (6u-1)/(2-6u)$. Our results for the lattice optimization are displayed in Table I together with those from measurement and previous calculations.

The A7 BZ is a distorted truncated octahedron (see Fig. 2). The distortions are relative to the trigonal direction (ΓT). Six of the eight hexagonal facets are irregular and the squared facets are rather isosceles trapezoids. The regular hexagons contain the T points and the irregular ones the L points. It is customary to consider a binary-bisectrix-trigonal system as indicated in Fig. 2. The high-symmetry directions ΓT, ΓL,

TABLE I. Structural parameters of bulk Bi. Compared are the present results with a previous calculation and experimental data (obtained at $T = 4.2$ K). d_{short} and d_{long} denote the short and long interlayer distances, respectively.

	a_r (Å)	α	u	d_{short} (Å)	d_{long} (Å)
LDA	4.67	57.94	0.236	1.606	2.267
GGA	4.93	56.18	0.232	1.621	2.513
LDA [25]	4.69	57.57	0.234	1.576	2.326
Expt. [46]	4.7236(5)	57.35(1)	0.23407(4)		

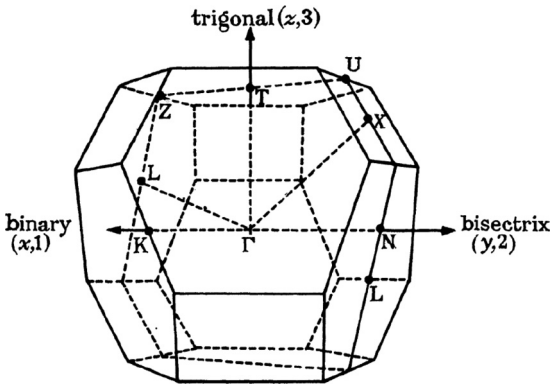

FIG. 2. The Brillouin zone of the A7 structure of bulk Bi. Figure is taken from Ref. [45].

ΓX, and the bisectrix direction lie in the mirror plane of the A7 structure, while the binary direction is perpendicular to it.

Figure 3 shows our calculated phonon dispersion curves along the bisectrix, trigonal, ΓX, binary, and ΓL directions together with the most comprehensive experimental data set

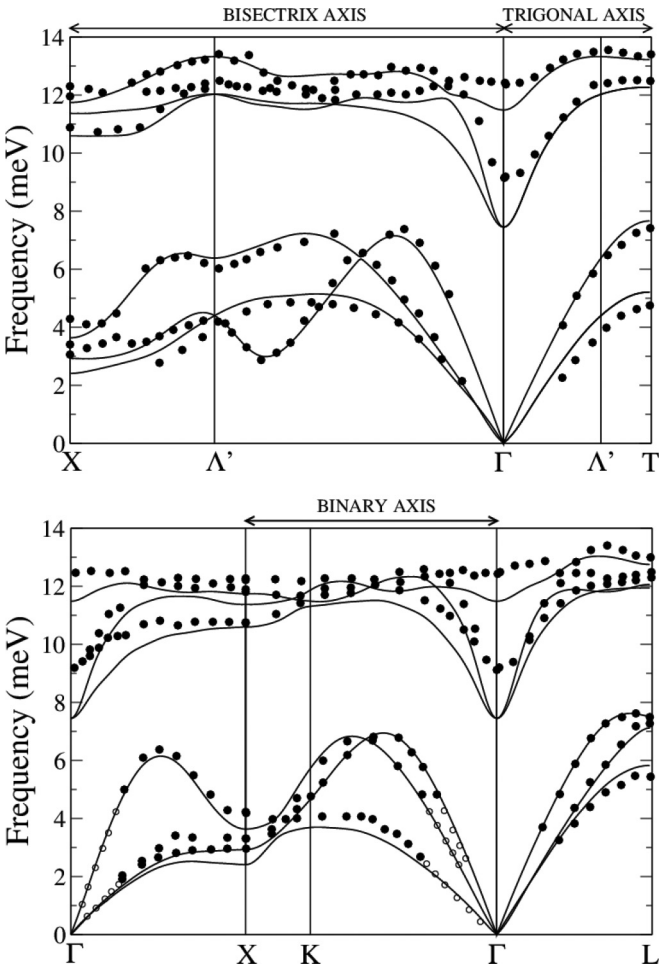

FIG. 3. Calculated phonon dispersion curves of bulk Bi along high-symmetry directions of the Brillouin zone. The black dots correspond to inelastic neutron scattering data taken at 75 K [47]. The point Λ' lies on the trigonal axis with $\mathbf{k}_{\Lambda'} = 2/3\mathbf{k}_{\mathrm{T}}$.

by MacFarlane [47] for comparison. The agreement with experimental data is quite good for the most part, especially regarding the acoustic branches. There are, however, some discrepancies for the lower optic branch, particularly around the zone center. These findings are in line with the previous theoretical study of the lattice dynamics of Bi by Díaz-Sánchez *et al.* [25]. Comparing calculations without and with SOC, they found that SOC clearly improves the description of the phonon dispersion, but with the exception of the optical branches near the Γ point.

A prominent feature of both experimental and theoretical spectra is the pronounced dip in the dispersion of the two lower optical branches at Γ, with a minimum frequency of about 9 meV found by inelastic neutron scattering and Raman experiments at low temperatures [47,48]. Such dips also occur in other group V elements (As, Sb) as well as in IV-VI compounds such as SnTe, and have been interpreted as caused by long-ranged interactions due to a resonant bonding effect in materials with pseudo-rocksalt structure [49]. Our calculation exaggerates this dip, a phenomenon well known from previous theoretical work [25]. We have checked that including the $5d$ semicore states in the valence space does not alter this feature. Furthermore, it was not changed by varying the Gaussian broadening, which indicates that Fermi-surface-related renormalization is not responsible for it. We observed, however, a high sensitivity on changes of the lattice structure, in particular on the internal structural parameter u. Using the experimental value of $u = 0.234$ instead of the optimized value 0.236 raises the lower and upper optical frequencies at Γ by 1.2 and 0.8 meV, respectively, thereby reducing the difference to the measured frequencies to less than 0.6 meV. Similar improvements are found for all optic branches.

We have performed calculations of the electron-phonon coupling constant in bulk Bi, given by

$$\lambda = \frac{1}{N(E_F)} \sum_{\mathbf{q}\nu} \sum_{\mathbf{k}ij} \frac{2}{\omega_{\mathbf{q}\nu}} |g^{\mathbf{q}\nu}(\mathbf{k}+\mathbf{q}j,\mathbf{k}i)|^2 \delta(\epsilon_{\mathbf{k}i} - E_F) \times \delta(\epsilon_{\mathbf{k}+\mathbf{q}j} - E_F). \quad (1)$$

Here, g denotes the screened electron-phonon coupling matrix elements, and the sum runs over all phonon modes (with momentum $\mathbf{q}$, branch index ν, and frequency $\omega_{\mathbf{q}\nu}$) and over all electronic states (with momentum $\mathbf{k}$, band index i, and energy $\epsilon_{\mathbf{k}i}$). $N(E_F)$ denotes the electronic density of states per spin at the Fermi energy E_F. Since the bulk Fermi surface consists of tiny Fermi pockets, care must be taken in the BZ sampling to assure a proper convergence. We have used meshes of up to $36\times36\times36$ k points for the electronic states and approximated the delta functions by Gaussians with widths of 0.1–0.2 eV. For the sum over phonon modes, the $12\times12\times12$ q-point mesh was applied. In all cases, we found $\lambda < 0.1$, which is consistent with the absence of superconductivity in bulk Bi down to 50 mK [7]. In a recent linear-response calculation using GGA, a very similar value of 0.09 was found [6].

B. Bi(111) geometry

The (111) surface of Bi is created by cutting the crystal perpendicular to the trigonal axis, i.e., parallel to the bilayers. It is energetically more favorable to cut the metallic (weak)

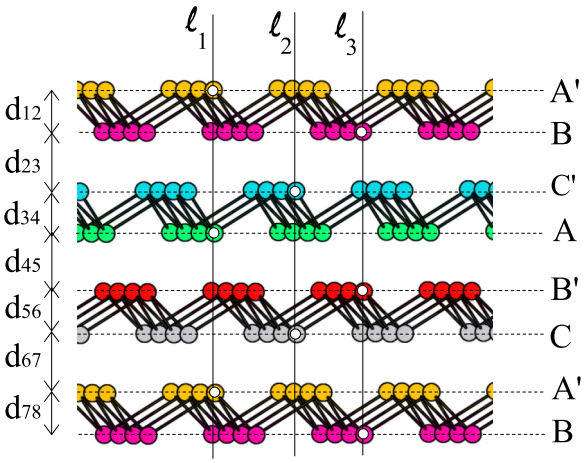

FIG. 4. (Color online) Side view of a sketch of the Bi(111) structure. A, A′, B, B′, C, and C′ represent the planes defined by each layer. The sticks connecting the balls are used to indicate only first-nearest neighbors (between atoms on planes A′ and B, C′ and A, or B′ and C) to highlight the bilayerlike structure of Bi(111). d_{ij} denotes the vertical spacing between adjacent planes.

bonds between bilayers and not the rather covalent (strong) bonds within a bilayer, which also explains its observed low reactivity [50]. Figure 4 sketches the resulting stacking of bilayers with its alternating short (d_{12}, d_{34}, etc.) and long (d_{23}, d_{45}, etc.) interlayer distances. Without relaxation they would equal the bulk interlayer spacings d_{short} and d_{long}, respectively. The stacking repeats itself after six atomic layers (three bilayers). As indicated by the vertical lines l_1, l_2, and l_3, atoms in every third atomic layer lie on top of each other. Bi(111) is a quite open surface, because the closest distance between atoms within a layer is rather large (4.54 Å) such that the surface leaves exposed even the third layer.

In bulk Bi, the intrabilayer distance is given by $d_{\text{short}} = 1.606$ Å, while the vertical interbilayer distance is $d_{\text{long}} = 2.267$ Å. Near the surface, these interlayer spacings are modified. Table II shows the calculated relaxation for three

TABLE II. Changes (%) in the interlayer spacing between the layers of clean Bi(111) films with respect to that in bulk Bi, $\Delta d_{i(i+1)}$. Given are the present results for three slabs of 6, 10, and 12 bilayers (BL). Changes in deeper interlayer spacings are below 0.1%. Shown are also values obtained in previous theoretical works and an experimental study. $T \rightarrow 0$ K values are estimates based on extrapolated values obtained at 140 K and higher temperatures.

	Theory					Experiment[a]	
	6 BL	10 BL	12 BL	6 BL[b]	7 BL[c]	$T = 140$ K	$T \rightarrow 0$ K
Δd_{12}	−1.62	−1.56	−1.56	−0.83	+0.6	+0.5±1.1	+1.2±2.3
Δd_{23}	1.37	1.32	1.32	+3.13	+6.2	+1.9±0.8	+2.6±1.7
Δd_{34}	−0.87	−0.93	−0.87			0.0±1.1	
Δd_{45}	0.13	0.18	0.13				
Δd_{56}	−0.25	−0.31	−0.31				

[a]Low-energy electron diffraction [51].
[b]GGA, pseudopotential plane-wave method [22].
[c]LDA, full-potential linearized augmented plane wave method [51].

different thicknesses of the slab (6, 10, and 12 bilayers) together with previous calculations [22,51] and low-energy electron diffraction (LEED) measurements [51]. Our results show a fast convergence of the relaxation with the slab thickness. Already for a 10-bilayer slab the interlayer distances are sufficiently converged, and the bulk spacing at the center of the slab is recovered. We found a shrinking of the first intrabilayer distance (d_{12}) of 1.56% and an expansion of the first interbilayer distance (d_{23}) of 1.32%. The first result is at variance with the LEED experiment, where an expansion of d_{12} was found, although the experimental error bars are large. Our value for d_{23}, however, agrees with the LEED result. Our pseudopotential results contrast a previous calculation using the full-potential linearized augmented plane-wave method, where both distances were found to expand [23], but a very large expansion of 6%–7% was predicted for d_{23} at variance with experiment. A recent pseudopotential calculation employing GGA found relaxations much closer to the present ones [22].

C. Bi(111) electronic structure

As indicated in Fig. 5, the tiny electron and hole pockets of bulk Bi are projected onto regions around the $\overline{M}$ and $\overline{\Gamma}$ points of the (111) surface BZ, respectively. In between, there are larger regions where the bulk spectrum possesses an energy gap near the Fermi level. As shown in Fig. 6, the electronic band structure of Bi(111) exhibits two surface localized bands along $\overline{\Gamma M}$ and part of the $\overline{\Gamma K}$ line, which fall into this energy-gap region. They are derived from two semirelativistic bands, one from each side of the slab. Since the surface electronic bands show a rather poor convergence with slab thickness, we performed calculations of the electronic band structure for 12, 24, and 36 bilayers of Bi(111). As shown in the previous subsection, these thicknesses are sufficient

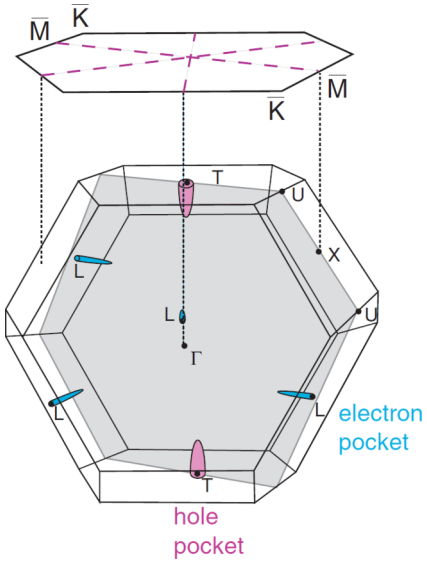

FIG. 5. (Color online) The projection of the bulk Brillouin zone of Bi onto the (111) surface. Sketched are the bulk Fermi surfaces (exaggerated in size). Figure is taken from Ref. [10]. The shaded area denotes the mirror plane.

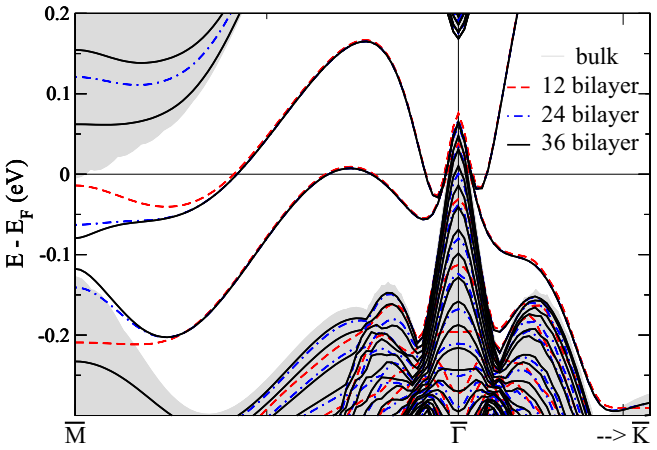

FIG. 6. (Color online) Surface band structure of a Bi(111) slab. Shown are the electronic bands in the vicinity of the Fermi energy for the 12-, 24-, and 36-BL slabs, respectively. The gray areas represent regions of bulk states.

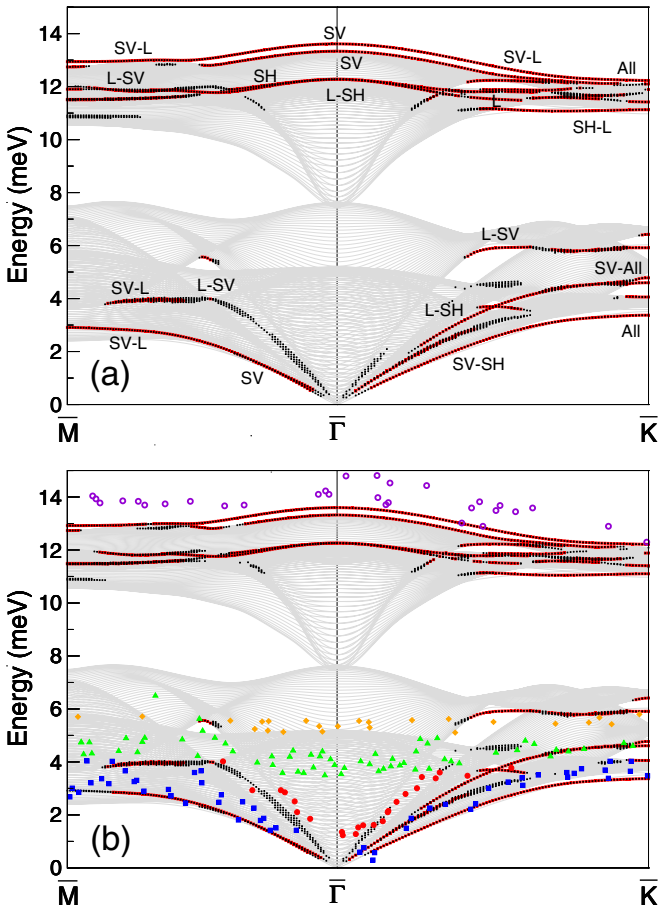

FIG. 7. (Color online) Phonon dispersion curves of a Bi(111) slab of 50 bilayers along the high-symmetry directions of the surface Brillouin zone obtained by slab filling of (a) a 6-bilayer and (b) a 12-bilayer slab. The dots correspond to surface modes whose amplitude weight in the two outermost bilayers is larger than 20% (red) or in the range 10%–20% (black). The light gray lines are bulk modes. In (a), the polarization of the surface modes away from the high-symmetry points is succinctly indicated with SV for shear vertical, L for longitudinal, and SH for shear horizontal or the word "All" if the polarization is not well defined. In (b), symbols correspond to peaks in inelastic helium atom scattering spectra taken at lower temperatures as reported by Tamtögl *et al.* [22].

to converge the interlayer distances at the surface and to recover the bulk spacing in the center of the slabs. In contrast, the surface electronic bands are not converged, but exhibit a sizable dependence on the film thickness in particular when approaching the $\overline{M}$ point. It was argued that for a semi-infinite surface, the two split bands should be degenerate at $\overline{M}$ on symmetry grounds [23,52]. However, in the case of finite slabs, such a degeneracy is not found. There is a strong hybridization between the upper and lower surface that does not allow convergence of the energy of these bands around $\overline{M}$ even for slabs of 36 bilayers or more [23]. In contrast, this intersurface interaction is much weaker away from $\overline{M}$, such that both electron and hole pockets are well converged already for a 12-bilayer Bi(111) slab. A more detailed analysis of the electronic structure and its dependence on the slab thickness will be published elsewhere [53]. Due to such a slow convergence, we will restrict the analysis of the electron-phonon induced self-energy effects (Sec. III E) to those parts of the $\overline{M\Gamma K}$ lines, where the surface band energies are sufficiently converged for a 12-bilayer slab.

D. Bi(111) surface phonons

We now address the lattice dynamics of the Bi(111) surface. Recently, three theoretical studies were devoted to surface phonons in the framework of the density functional theory [6,26,27]. Due to the heavy numerical work involved in dealing with SOC, these calculations were performed only for thin slabs up to 6 bilayers, where the vibrational spectrum exhibited significant variations as a function of thickness. As we are primarily interested in the properties of a semi-infinity Bi(111) surface we checked the convergence of the surface localized vibrations by performing lattice dynamics calculations for 6- and 12-bilayer slabs, respectively. In both cases, the slabs were relaxed and SOC was taken into account. Surface phonon spectra were then obtained by combining the real-space force constants of the slab with those from the bulk calculation to simulate the dynamics of an asymmetric slab of 50 bilayers. An asymmetric slab contains one surface taken from the fully relaxed slab, while the other surface corresponds to the ideal bulk-truncated case. The phonon spectrum of such a slab thus contains surface modes related to both types of surfaces. From the components of each eigenvector, one can determine the vibrational weight at each atomic site and at each direction. Figure 7 shows the phonon dispersions based on the 6- and 12-bilayer calculations, respectively. The optic and acoustic parts of the projected bulk bands (gray lines) slightly touch each other at $\overline{\Gamma}$ because the lower optic bulk mode at the zone center has such a small calculated frequency. Surface localized modes of the true (relaxed) surface are identified by their vibrational weight in the first two bilayers at the surface. Modes with a weight of more than 20% are highlighted in red, while those with a weight between 10% and 20% are indicated by black dots. A more detailed characterization of surface modes at the high-symmetry points $\overline{\Gamma}$, $\overline{M}$, and $\overline{K}$ is given in Table III.

TABLE III. Surface localized phonons of Bi(111) at high-symmetry points of the surface Brillouin zone for a slab of 50 BL obtained with the slab-filling procedure. Frequencies (in meV) and dominant polarization are shown with respect to the propagation vector. For modes at $\overline{\Gamma}$ and $\overline{M}$, the polarization is indicated by SV for shear vertical, L for longitudinal, and SH for shear horizontal, while the subscripts indicate the layers with larger weight, starting with the outermost surface layer. RW denotes the Rayleigh wave. For $\overline{K}$, modes show a more complex polarization pattern, which is therefore not shown. Our values are compared with available data from helium atom scattering experiment and theoretical slab calculations. In the latter cases, no slab filling was performed.

			Theory	
Point	This work	Experiment[a]	5 BL[b]	6 BL[c]
$\overline{\Gamma}$	12.3 (L_{1-6})		11.8, 12.2	
	12.3 (SH_{1-6})			
	13.3 (SV_{3-6})			14.2
	13.6 ($SV_{1,2}$)	14–15	13.6	15.3
$\overline{M}$	2.9 (RW, $SV_2 + L_1$)	≈3		
	11.5 ($SV_{1,2} + L_{1,2}$)		≈11.5	
	12.7 ($SV_{3-8} + L_{3-8}$)			
	12.9 ($SV_{1,2} + L_2$)	≈ 14	≈ 13	
$\overline{K}$	3.4 (RW)	≈ 3.8		
	4.1, 4.6, 4.8, 5.9, 6.4			
	11.1, 11.4, 11.8, 12.2	≈ 12.3		

[a]Helium atom scattering data from Tamtögl *et al.* [22], taken from their low-temperature data of Fig. 4(a).
[b]LDA pseudopotential calculation by Chis *et al.* [26]. Values shown for $\overline{M}$ are estimates based on their Fig. 3.
[c]GGA pseudopotential calculation without spin-orbit interaction [22].

One can note that after the slab-filling procedure, both calculations give essentially the same surface localized spectrum. This indicates that changes in the real-space force constants due to the presence of the surface are essentially confined to the outer two or three bilayers and are reasonably well converged already for the 6-bilayer slab. The fast convergence of the dynamical properties contrasts the very slow convergence of the surface electronic band structure. This indicates that the uncertainty in the surface band structure near the $\overline{M}$ point has little influence on the electronic response to atomic perturbations and hardly affects the frequencies of the surface phonons.

A prominent feature of the Bi(111) surface phonon dispersion is the appearance of modes above the optic bulk band almost everywhere along the $\overline{\Gamma M}$ and $\overline{\Gamma K}$ directions. The upper branch consists of predominately vertical vibrations of atoms in the first bilayer, and reflects a 12% stiffening of the force constants between the two layers forming the first bilayer and the contraction of the corresponding interlayer spacing (see Table II). The second highest branch above the optic bulk spectrum also has a shear vertical polarization but is mainly localized in the second and third bilayers. A third surface branch with in-plane (shear-horizontal and longitudinal) polarization is present within the optic bulk spectrum and is localized over the first three bilayers.

In the acoustic spectrum, the Rayleigh wave (RW) falls slightly below the bulk band along $\overline{\Gamma K}$, while it remains within the bulk continuum along $\overline{\Gamma M}$. Along $\overline{\Gamma K}$, above the RW, there appear several modes localized primarily in the first bilayer. The surface mode at about 6 meV stretching from $\overline{K}$ halfway to $\overline{\Gamma}$ involves vibrations of atoms in the second bilayer with mainly shear vertical and to a lesser extent in-plane polarization. Along the $\overline{\Gamma M}$ direction, the longitudinal first-bilayer mode lying above the RW shows a weaker localization near $\overline{\Gamma}$, but when approaching $\overline{M}$ it becomes more localized and acquires a stronger vertical component.

The surface phonons have been recently investigated via inelastic helium atom scattering (HAS) by Tamtögl *et al.* [22]. In Fig. 7(b), we have added the reported frequencies taken at lower temperatures ($T = 103/123$ K). They clearly observed surface modes above the optic bulk band and interpreted their data as evidence for two branches with shear vertical polarization, in agreement with our calculation. Their frequencies are about 1 meV higher than our theoretical result, but also lies significantly above the experimental bulk maximum of ≈13.5 meV (see Fig. 3). In the acoustic part, good agreement between our calculations and the HAS results are found for the RW and the longitudinal first-bilayer mode as well as the second-bilayer mode at about 6 meV.

In the HAS spectra, a variety of additional peaks were observed in the range of 4–5 meV, most prominent near $\overline{\Gamma}$. They were interpreted as caused by longitudinally polarized vibrations in the third layer (second bilayer). This interpretation was based on the theoretical vibrational spectrum of a 6-bilayer slab and supported by calculations of the charge density variations induced by such vibrations, which were found to be large enough at the scattering point of the helium atom to explain the observed HAS peaks.

When we consider the 12-bilayer slab, we do find similar vibrational modes in this energy range with enhanced longitudinal polarization in the third and fourth layers. However, this enhanced vibrational weight is a property of thin slabs only. When simulating the dynamics of thicker slabs by the slab-filling procedure, the weight becomes successively smaller with increasing thickness. It remains an open question, if the density oscillations related to these modes remain strong enough in the limit of thick slabs to explain the HAS peaks, which have been observed for Bi(111) samples of macroscopic thickness.

The presence of low-frequency optical modes causes the surface atoms to have an enhanced vibrational density of states at lower frequencies. Figure 8 shows the layer-projected phonon density of states (LDOS) for the first, second, and twelfth layers of the 12-bilayer slab. The twelfth layer is deep enough so that it undergoes no relaxation (see Table II) and thus its LDOS is representative of the phonon DOS of bulk Bi. Figure 8 shows that the LDOS of the first two layers has an additional peak at the upper end of the optical spectrum as compared to the bulk due to the presence of the superbulk surface modes. In contrast, the acoustic part of their LDOS is softened with respect to the bulk, which can be traced back to a softening of the nearest-neighbor coupling within the first layer. For each LDOS curve, the Debye-type behavior applies in the beginning of the spectrum. From the initial quadratic behavior, we deduce a Debye cutoff frequency of 8.9 meV for the bulk and of 7.3 meV for the first and second surface layers, respectively. These values are fairly consistent

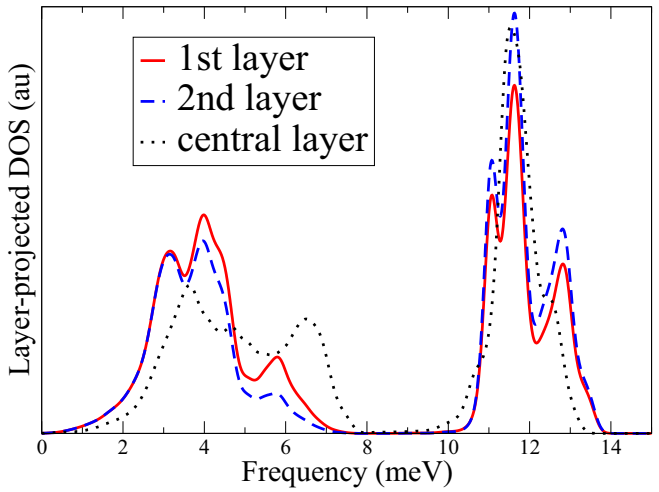

FIG. 8. (Color online) Layer-projected phonon density of states (LDOS) obtained for a 12-bilayer Bi(111) slab. The red (full) and blue (dashed) lines show the LDOS of the first and second layers of the outermost bilayer, respectively. The black (dotted) curve corresponds to a central bilayer and represents a bulklike spectrum.

with experimental Debye frequencies of about 10 meV for the bulk [14,54] and 6.5 meV for the Bi(111) surface layer. The latter value was deduced from measurements of the mean-square atomic vibrational amplitudes of the surface atoms [51]. The Debye model is often used as an approximation for the Eliashberg function describing the coupling of an electronic state to the phonon system. We will show in the following section, however, that the spectral shape of the coupling function can deviate significantly from the simple Debye form for the surface electronic states of Bi(111).

E. Electron-phonon interaction

The metallic character of the Bi(111) surface gives the opportunity of studying the *e*-ph interaction for states which are well confined at the surface and subject to a strong spin-orbit interaction. To quantify the strength of the electron-phonon interaction, the dimensionless *e*-ph coupling parameter is used:

$$\lambda_{\mathbf{k}i} = \int_0^{\omega_{\max}} \frac{\alpha^2 F^{\mathrm{E}}_{\mathbf{k}i}(\omega) + \alpha^2 F^{\mathrm{A}}_{\mathbf{k}i}(\omega)}{\omega} d\omega. \qquad (2)$$

Here, $\mathbf{k}i$ denotes an electron (hole) state momentum and band index, $\omega_{\max}$ is the maximum phonon frequency, and $\alpha^2 F^{\mathrm{E(A)}}_{\mathbf{k}i}(\omega)$ is the electronic state dependent Eliashberg spectral function corresponding to phonon emission (E) and absorption (A) processes [55]:

$$\alpha^2 F^{\mathrm{E(A)}}_{\mathbf{k}i}(\omega) = \sum_{\mathbf{q}\nu, f} \delta(\epsilon_{\mathbf{k}i} - \epsilon_{\mathbf{k}+\mathbf{q}f} \mp \omega_{\mathbf{q}\nu}) \times |g^{\mathbf{q}\nu}(\mathbf{k}+\mathbf{q}f, \mathbf{k}i)|^2 \delta(\omega - \omega_{\mathbf{q}\nu}). \qquad (3)$$

The "−" and "+" signs in the delta function with electron energies correspond to phonon emission and absorption, respectively. The sum is carried out over final electronic states (f) and phonon modes ($\mathbf{q}\nu$).

In the calculation of the *e*-ph coupling, a 12-bilayer Bi(111) film is used, and only those states in the surface electronic bands that do not differ in energy from those of the 24- and 36-bilayer calculations are considered, i.e., we restrict our analysis to momenta in the range $\sim 0.6|\overline{\Gamma M}|$). To see how the surface electronic states couple to phonons, we have calculated $\lambda_{\mathbf{k}i}$ for different electron (hole) energies and momenta. The summation over phonons in Eq. 3 was carried out over 1296 wave vectors (36 × 36) in the surface BZ. The delta function with electronic energies was approximated by a first-order Hermite-Gaussian function with a smearing width in the range of 0.07–0.4 eV.

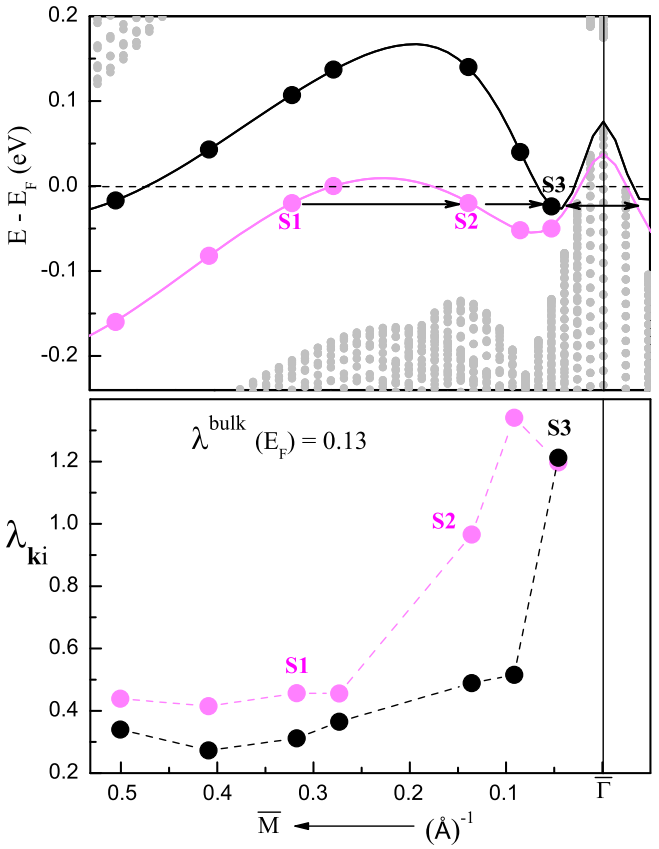

FIG. 9. (Color online) (Top) Thick circles indicate the surface electronic states for which the electron-phonon coupling calculations were done. S1, S2, and S3 denote specific surface states of similar binding energies, which are discussed in the text in more detail. Bulk Bi bands projected onto the (111) plane are indicated by small gray circles. (Bottom) Electron-phonon coupling parameter $\lambda_{\mathbf{k}i}$ as a function of electron (hole) momentum along the $\overline{\Gamma M}$ symmetry direction for electronic states in the lower (gray/purple) and higher (black) surface bands.

The electron-phonon parameter $\lambda_{\mathbf{k}i}$ as a function of momentum is shown in Fig. 9 for the two surface bands. The electron-phonon coupling near the Fermi level is of intermediate strength ($\lambda \approx 0.45$, the lower state) unless the electronic state lies close to $\overline{\Gamma}$. It is markedly different from the very weak coupling constant of $\lambda < 0.1$ found at the Fermi level of bulk Bi (see Sec. III A). The strength of *e*-ph coupling for excited electrons on Bi(111) is also higher than the values of $\lambda_{\mathbf{k}i} = 0.2$–$0.3$ obtained for the surface electronic states near the Fermi level on the Bi(100) and Bi(110) surfaces [5,17].

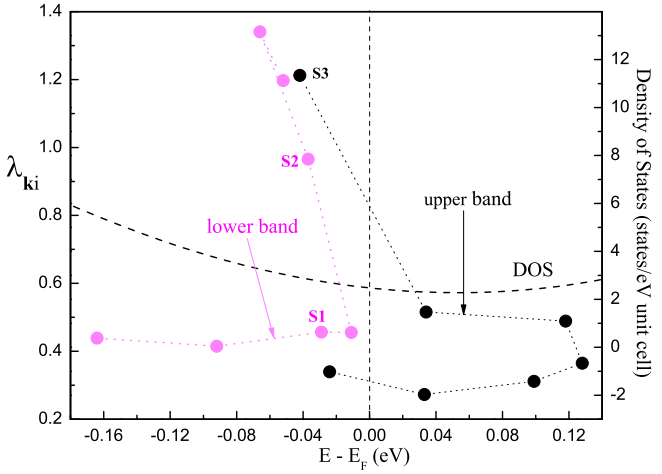

FIG. 10. (Color online) Electron-phonon coupling parameter λ_{ki} as a function of electron energy. The notation is the same as in Fig. 9. The points are connected according to their positions in the $\overline{\Gamma M}$ direction. The dashed line shows the calculated density of electronic states $N(E)$ as a function of energy.

Due to a small energy range covered by the surface states (∼0.15 eV around E_F) the coupling strength is not expected to vary considerably with electron momentum if the scattering within the surface bands dominates. That is the case at large electron momentum. As is evident from Fig. 9, for $|\mathbf{k}| > 0.2|\overline{\Gamma M}|$ the calculated λ_{ki} shows a weak dependence on electron momentum and the strength of the *e*-ph interaction varies between 0.3 and 0.5 for both electronic bands, i.e., it is not large for either of the two. There is also an indication of a rather weak dependence on the electron binding energy, namely, the difference in the coupling strength between the two electronic bands at the same $\mathbf{k}$ is small and does not exceed 0.15. In order to illustrate this, λ_{ki} as a function of binding energy is shown in Fig. 10.

However, when $\mathbf{k}$ approaches the $\overline{\Gamma}$ point the strength of *e*-ph interaction increases significantly. It reaches up to 1.2–1.4 in both surface bands. Furthermore, the *e*-ph coupling becomes very sensitive to the energy position of a hole (electron) state in the surface band. At the same electron momentum, λ_{ki} in the lower surface band can be more than twice as large as in the higher band.

In the case of Bi(100) surface, the strong energy dependence of λ_{ki} was explained by simple phase space arguments with the assumption of a weak energy dependence of the *e*-ph matrix elements [5]. Here, this argument is not valid. To illustrate that, Fig. 10 shows the calculated density of electronic states (DOS). In the surface-state energy range, the density of states is a smooth curve which does not reproduce the variation of λ_{ki}. Only for hole states with large momentum in the upper surface band the strength of *e*-ph coupling is determined to a certain extent by the available phase space.

The scattering processes leading to such a strong *e*-ph interaction at small electron momenta can be derived from the corresponding spectral functions. Figure 11 shows the Eliashberg functions calculated for surface states S1, S2, and S3 (see Figs. 9 and 10), which have similar binding energies but different electron momenta. Only the average of the emission and adsorption spectral function is shown because both parts nearly coincide.

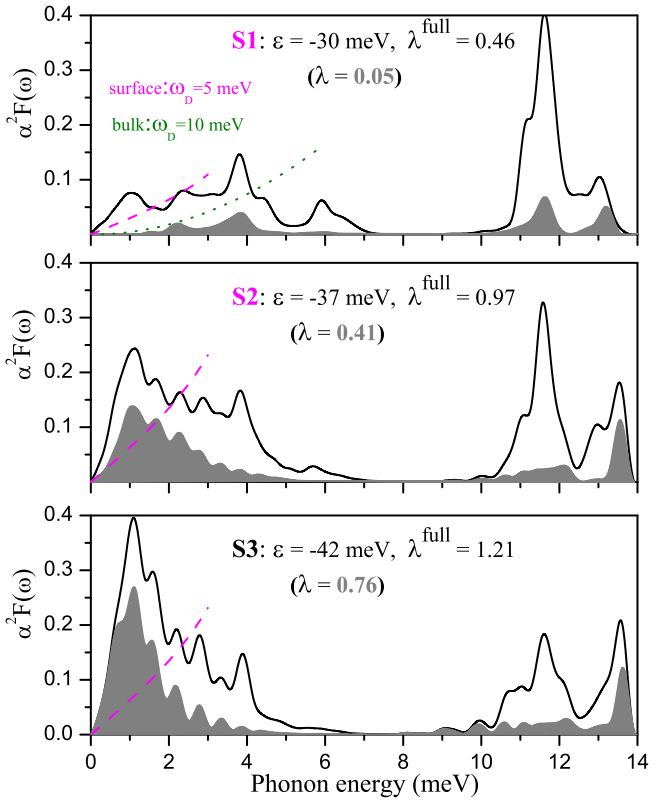

FIG. 11. (Color online) Average of the absorption and emission spectral functions $\alpha^2 F_{ki}(\omega)$, calculated for surface electronic states S1, S2, and S3 (see Fig. 9). The gray areas show the contribution of electronic transitions to the $\overline{\Gamma}$ point region (Fig. 9). The dashed (dotted) line indicates the initial slope of a Debye spectrum assuming a surface (bulk) Debye frequency of 5 meV (10 meV) and scaled by the corresponding coupling constant.

A distinctive feature of all $\alpha^2 F_{ki}(\omega)$ shown in Fig. 11 is a large weight at low energies, which is related to lattice vibrations with small energies (and small wave vectors) even though their contribution to the phonon density of states is negligible (Fig. 8). The type of transitions they are connected to depends on the momentum position of the electronic state in the surface bands. In the case of state S1, the peak in the spectral function at ∼1 meV is related to the nearest intraband transitions. With decreasing electron momentum (S1→S2→S3), the small energy peak caused by the intraband scattering remains, but in addition the possibility of scattering to electronic states near the $\overline{\Gamma}$ point increases. Such transitions via long-wavelength phonons with small energies give a large contribution to the coupling constant λ according to its definition [Eq. (2)]. The latter contribution increases rapidly as the electron momentum approaches the $\overline{\Gamma}$ point and is responsible for the sharp increase of λ_{ki} at small electron momentum and at energies, where electronic states around the $\overline{\Gamma}$ point are available for phonon-mediated transitions. These states are essentially bulklike. Specifically, while the dispersion of the two bands of the surface states (Fig. 9) suggests that they rise above the Fermi level when approaching

$\overline{\Gamma}$, in reality both bands quickly acquire a bulklike character, and a true surface localized state at $\overline{\Gamma}$ appears at much lower energies (≈ 350 meV below E_F). Thus, states near $\overline{\Gamma}$ involved in the small-momentum transitions are bulklike. This low-frequency contribution clearly increases the coupling strength, but it is also associated with a larger uncertainty because for the present 12-bilayer slab, the bulk-projected part is represented only by a few bands in this energy region. Calculations with much thicker slabs would be required for proper convergence of this contribution, which is currently not feasible.

Attempts to measure the coupling strength of Bi(111) surface states focused on the part of the hole pocket closest to $\overline{\Gamma}$, which corresponds approximately to our state S2. From measurements of the self-energy, Ast and Höchst extracted coupling constants of $\lambda = 0.6 \pm 0.05$ and 2.3 ± 0.2 when approximating the Eliashberg function by a Debye spectrum with either bulk ($\omega_D = 10$ meV) or surface Debye frequencies ($\omega_D = 5$ meV), respectively [14]. Kirkegaard *et al.* later argued that by taking into account the finite spectrometer energy resolution, these values should be corrected down to couplings of the order 0.4 [17]. Such a value was obtained by Gayone *et al.* from data on temperature-dependent momentum distribution curves near the Fermi level crossing [18]. This analysis was also based on a Debye model for the Eliashberg function.

The unusual shape of the calculated spectral functions, in particular for the S2 and S3 states, renders the applicability of the Debye model rather questionable. As shown by the dashed lines in Fig. 11, the Debye approximation [56] misses the strong enhancement of $\alpha^2 F_{\mathbf{k}i}(\omega)$ at $\omega \approx 1$ meV. On contrast, the Debye model might be more appropriate for an analysis in the momentum region $k \approx (0.3\text{–}0.5)|\overline{\Gamma M}|$, where this low-energy peak is not very pronounced. For example, the initial slope of the Eliashberg function for the S1 state is reasonably well described by the Debye model if the surface Debye frequency of 5 meV is used (Fig. 11).

IV. SUMMARY

We have performed a comprehensive investigation of the structural, electronic, lattice dynamical, and electron-phonon coupling properties of the Bi(111) surface within density functional perturbation theory, taking into account the spin-orbit coupling consistently. Although some details of the electronic structure of Bi(111) depend on the slab thickness, we found that the lattice dynamics of Bi(111) is practically converged already for slabs of 6 bilayers. Changes in the dynamical couplings are confined essentially to interatomic bonds in the first two bilayers, where also the main structural relaxation occurs. The surface phonon spectrum exhibits superbulk modes which lie above the bulk spectrum. In addition, the layer-projected vibrational density of states is enhanced at lower frequencies for the first bilayer, consistent with the observed enhanced average vibrational amplitudes of the surface atoms. A calculation of electronic-state-dependent coupling to phonons gave moderate coupling strengths of 0.45 for surface states with larger momenta. Surface states close to $\overline{\Gamma}$ are predicted to have significantly higher couplings of the order of 1. This increase is connected to an enhanced scattering via phonons with long wavelengths and small energies into bulklike electronic states near $\overline{\Gamma}$. The calculated coupling for states of the hole Fermi surface closest to $\overline{\Gamma}$ is about twice as large as those deduced from experiment. This discrepancy may be partly due to insufficient thickness of the slab, but also may result from an inappropriate assumption in the experimental analysis. We found that the state-dependent Eliashberg functions strongly deviate in shape from that of a Debye model, indicating that the use of the latter in an analysis of electronic self-energies from photoemission spectra is not justified and likely fails to give correct results for the coupling strength.

ACKNOWLEDGMENT

The work of M.A.O. and T.S.R. was partially funded by US Department of Energy, DE-FG02-07ER46354.

[1] D. Shoenberg, Proc. R. Soc. A **170**, 341 (1939).
[2] B. Weitzel and H. Micklitz, Phys. Rev. Lett. **66**, 385 (1991).
[3] A. B. Shick, J. B. Ketterson, D. L. Novikov, and A. J. Freeman, Phys. Rev. B **60**, 15484 (1999), and references therein.
[4] D.-K. Seo and R. Hoffmann, J. Solid State Chem. **147**, 26 (1999).
[5] J. E. Gayone, S. V. Hoffmann, Z. Li, and Ph. Hofmann, Phys. Rev. Lett. **91**, 127601 (2003).
[6] G. Q. Huang and J. Yang, J. Phys.: Condens. Matter **25**, 175004 (2013).
[7] M. Tian, N. Kumar, M. H. W. Chan, and T. E. Mallouk, Phys. Rev. B **78**, 045417 (2008).
[8] T. T. Chen, J. D. Leslie, and H. J. T. Smith, Physica (Amsterdam) **55**, 439 (1971).
[9] R. Heid, K. P. Bohnen, I. Y. Sklyadneva, and E. V. Chulkov, Phys. Rev. B **81**, 174527 (2010).
[10] Ph. Hofmann, Prog. Surf. Sci. **81**, 191 (2006).
[11] G. Jezequel, Y. Petroff, R. Pinchaux, and F. Yndurain, Phys. Rev. B **33**, 4352 (1986).
[12] M. Hengsberger, P. Segovia, M. Garnier, D. Purdie, and Y. Baer, Eur. Phys. J. B **17**, 603 (2000).
[13] Ch. R. Ast and H. Höchst, Phys. Rev. Lett. **87**, 177602 (2001).
[14] Ch. R. Ast and H. Höchst, Phys. Rev. B **66**, 125103 (2002).
[15] Ch. R. Ast and H. Höchst, Phys. Rev. B **70**, 245122 (2004).
[16] Yu. M. Koroteev, G. Bihlmayer, J. E. Gayone, E. V. Chulkov, S. Blügel, P. M. Echenique, and Ph. Hofmann, Phys. Rev. Lett. **93**, 046403 (2004).
[17] C. Kirkegaard, T. K. Kim, and Ph. Hofmann, New J. Phys. **7**, 99 (2005).
[18] J. E. Gayone, C. Kirkegaard, J. W. Wells, S. V. Hoffmann, Z. Li, and Ph. Hofmann, Appl. Phys. A **80**, 943 (2005).
[19] Ph. Hofmann, I. Yu. Sklyadneva, E. D. L. Rienks, and E. V. Chulkov, New J. Phys. **11**, 125005 (2009).
[20] I. Y. Sklyadneva, G. Benedek, E. V. Chulkov, P. M. Echenique, R. Heid, K. P. Bohnen, and J. P. Toennies, Phys. Rev. Lett. **107**, 095502 (2011).

[21] A. Tamtögl, M. Mayrhofer-Reinhartshuber, N. Balak, W. E. Ernst, and K. H. Rieder, J. Phys.: Condens. Matter **22**, 304019 (2010).
[22] A. Tamtögl, P. Kraus, M. Mayrhofer-Reinhartshuber, D. Campi, M. Bernasconi, G. Benedek, and W. E. Ernst, Phys. Rev. B **87**, 035410 (2013).
[23] Y. M. Koroteev, G. Bihlmayer, E. V. Chulkov, and S. Blügel, Phys. Rev. B **77**, 045428 (2008).
[24] É. D. Murray, S. Fahy, D. Prendergast, T. Ogitsu, D. M. Fritz, and D. A. Reis, Phys. Rev. B **75**, 184301 (2007).
[25] L. E. Díaz-Sánchez, A. H. Romero, and X. Gonze, Phys. Rev. B **76**, 104302 (2007).
[26] V. Chis, G. Benedek, P. M. Echenique, and E. V. Chulkov, Phys. Rev. B **87**, 075412 (2013).
[27] J. Yang, G. Q. Huang, and X. F. Zhu, Phys. Status Solidi B **250**, 1937 (2013).
[28] G. Benedek, M. Bernasconi, K.-P. Bohnen, D. Campi, E. V. Chulkov, P. M. Echenique, R. Heid, I. Yu. Sklyadneva, and J. P. Toennies, Phys. Chem. Chem. Phys. **16**, 7159 (2014).
[29] L. Hedin and B. I. Lundqvist, J. Phys. C: Solid State Phys. **4**, 2064 (1971).
[30] J. P. Perdew, K. Burke, and M. Ernzerhof, Phys. Rev. Lett. **77**, 3865 (1996).
[31] D. Vanderbilt, Phys. Rev. B **32**, 8412 (1985).
[32] S. G. Louie, K. M. Ho, and M. L. Cohen, Phys. Rev. B **19**, 1774 (1979).
[33] B. Meyer, C. Elsässer, and M. Fähnle, FORTRAN90 Program for Mixed-Basis Pseudopotential Calculations for Crystals, Max-Planck-Institut für Metallforschung, Stuttgart.
[34] L. Kleinman, Phys. Rev. B **21**, 2630 (1980).
[35] W. H. Press, S. A. Teukolsky, W. T. Vetterling, and B. P. Flannery, *Numerical Recipes in Fortran, The Art of Scientific Computing*, 2nd ed. (Cambridge Cambridge University Press, Cambridge, UK, 1992).
[36] T. Björkman, A. Gulans, A. V. Krasheninnikov, and R. M. Nieminen, J. Phys.: Condens. Matter **24**, 424218 (2012).
[37] A. Ramirez-Torres, D. Le, and T. S. Rahman (unpublished).
[38] A. Marini, P. García-González, and A. Rubio, Phys. Rev. Lett. **96**, 136404 (2006).
[39] N. E. Zein, Fiz. Tverd. Tela (Leningrad) **26**, 3028 (1984) [Sov. Phys.–Solid State **26**, 1825 (1984)].
[40] S. Baroni, P. Giannozzi, and A. Testa, Phys. Rev. Lett. **58**, 1861 (1987).
[41] R. Heid and K. P. Bohnen, Phys. Rev. B **60**, R3709 (1999).
[42] P. Giannozzi, S. de Gironcoli, P. Pavone, and S. Baroni, Phys. Rev. B **43**, 7231 (1991).
[43] R. Heid and K. P. Bohnen, Phys. Rep. **387**, 151 (2003).
[44] M. S. Dresselhaus, in *The Physics of Semimetals and Narrow-gap Semiconductors, Proceedings of the Conference, Dallas, Texas, 20-21 March 1970*, Journal of Physics and Chemistry of Solids, Supplement No. 1, Vol. 32 (Pergamon Press, New York, 1971), p. 3.
[45] A. P. Jeavons and G. A. Saunders, Proc. R. Soc. A. **310**, 415 (1969).
[46] D. Schiferl and C. S. Barrett, J. Appl. Crystallogr. **2**, 30 (1969).
[47] R. E. MacFarlane, in *The Physics of Semimetals and Narrow-gap Semiconductors, Proceedings of the Conference, Dallas, Texas, 20-21 March 1970*, Journal of Physics and Chemistry of Solids, Supplement No. 1, Vol. 32 (Pergamon Press, New York, 1971), p. 289.
[48] J. Höhne, U. Wenning, H. Schultz, and S. Hüfner, Z. Phys. B **27**, 297 (1977).
[49] S. Lee, K. Esfarjani, T. Luo, J. Zhou, Z. Tian, and G. Chen, Nat. Commun. **5**, 3525 (2014).
[50] F. Jona, Surf. Sci. **8**, 57 (1967).
[51] H. Mönig, J. Sun, Y. M. Koroteev, G. Bihlmayer, J. Wells, E. V. Chulkov, K. Pohl, and P. Hofmann, Phys. Rev. B **72**, 085410 (2005).
[52] T. Hirahara, T. Nagao, I. Matsuda, G. Bihlmayer, E. V. Chulkov, Yu. M. Koroteev, P. M. Echenique, M. Saito, and S. Hasegawa, Phys. Rev. Lett. **97**, 146803 (2006).
[53] M. Alcántara Ortigoza *et al.* (unpublished).
[54] K. G. Ramanathan and T. M. Srinivasan, Phys. Rev. **99**, 442 (1955).
[55] G. Grimvall, *The Electron-Phonon Interaction in Metals* (North-Holland, New York, 1981).
[56] We used the $2D_2$ model of B. Hellsing, A. Eiguren, and E. V. Chulkov, J. Phys.: Condens. Matter **14**, 5959 (2002).